Atmos. Meas. Tech. Discuss., doi:10.5194/amt-2016-169, 2016
Manuscript under review for journal Atmos. Meas. Tech.
Published: 9 August 2016

Atmospheric Measurement Techniques Discussions

Cloud Detection in All-Sky Images via Multi-scale Neighborhood Features and Multiple Supervised Learning Techniques

Hsu-Yung Cheng [a*] , Chih-Lung Lin [b]

[a]Department of Computer Science and Information Engineering, National Central University. No.300 Jhongda Rd., Jhongli City, Taoyuan 32001, Taiwan

[b]Department of Electronic Engineering, Hwa Hsia University of Technology, Taiwan

***Abstract*: Cloud detection is important for providing necessary information such as cloud cover in many applications. The classic method for cloud detection is based on thresholding of the red blue ratio of an image pixel. However, it is difficult to select a suitable threshold for all cloud conditions. Also, the desired thresholds for different all-sky cameras are different. In this paper, we propose to perform cloud detection using supervised learning techniques. The features are extracted from local image patches with different sizes to include local structure and multi-resolution information. The cloud models are learned through the training process. We consider classifiers including random forest, support vector machine and Bayesian classifier. To take advantage of the clues provided by multiple classifiers and various levels of patch sizes, we employ a voting scheme to combine the results to further increase the detection accuracy. In the experiments, we have shown that the proposed method can distinguish cloud and non-cloud pixels more accurately compared with existing works.**

***Keywords*: All-sky Image; Cloud Detection; Multi-resolution; Classifier; Supervised Learning**

[*] Corresponding author. Tel.: +886-3-4227151 ext35306, fax: +886-3-422-2681
Email address: chengsy@csie.ncu.edu.tw

Atmos. Meas. Tech. Discuss., doi:10.5194/amt-2016-169, 2016
Manuscript under review for journal Atmos. Meas. Tech.
Published: 9 August 2016

Atmospheric Measurement Techniques Discussions

1 Introduction

With the trend of sustainable and green energy, there is a growing demand for solar energy technology. To utilize solar energy effectively, integrated and large scale photovoltaic systems need to overcome the unstable nature of solar resource (Gueymard, 2004; Heinemann et al., 2006; Lorenz et al., 2009). The ability to forecast surface solar irradiance is helpful for planning and deployment of electricity generated by different units. Numerical weather prediction information or satellite images are popular materials used for wide-range prediction (Marquez and Coimbra, 2011; Perez et al., 2002; Perez et al., 2010; Remund et al., 2008). However, the resolution of prediction with respect to space and time obtained by weather prediction information or satellite cloud images is relatively coarse compared to the resolution desired for photovoltaic grid operators. For more refined spatial and temporal resolution of irradiance prediction, researches that analyze images obtained from devices capturing skies have emerged. Ground-based sky camera systems have been proposed to capture the images of the sky (Sabburg and Wong, 1999), allowing researchers to study the relationship between the sun and clouds and the effect of clouds. Devices developed more recently include Whole Sky Imager (Kassianov et al., 2005; Li et al., 2004), Whole Sky Camera (Long et al., 2006), All-Sky Imager (Kubota et al., 2003), and Total Sky Imager (Calbo and Sabburg, 2008; Long et al., 2006; Pfister et al., 2003). These devices are useful to make up the deficiency of satellite cloud observations in terms of spatial and temporal resolutions.

Cloud coverage, configurations and types are critical factors that influence the solar irradiance (Cazorla et al. 2008). A category of research works are devoted to detecting, classifying (Heinle et al., 2010; Martínez-Chico et al., 2011), and tracking clouds (Marquez and Coimbra, 2013; Tapakis and Charalambides, 2013; Wood-Bradley et al., 2012). The relationships between cloud coverage and surface solar irradiance have been explored (Feister and Shields, 2005; Fu and Cheng, 2013; Pfister et al., 2003). It has been shown that cloud fraction and surface irradiance are negatively correlated under most conditions. In addition to providing cloud coverage information, accurate cloud detection result could further improve the cloud type classification accuracy (Cheng and Yu, 2015). It has been

Atmos. Meas. Tech. Discuss., doi:10.5194/amt-2016-169, 2016
Manuscript under review for journal Atmos. Meas. Tech.
Published: 9 August 2016

Atmospheric Measurement Techniques Discussions

established that employing cloud type information in the process of short-term irradiance prediction cloud yield more accurate prediction results (Cheng and Yu, 2015).

Cloud detection in all-sky image is to decide if a pixel belongs to a cloud. Traditionally, red blue ratio (RBR) of each pixel is used to indicate whether the dominant source of the pixel is from clear sky or clouds (Chow et al., 2011; Johnson et al., 1989, 1991; Long et al., 2006; Shields et al., 2007, 2009). Then, a threshold is applied to RBR to determine cloud pixels in a sky image. The pixels whose RBRs are lower than the threshold are classified as clear sky and the pixels whose RBRs are higher the threshold are labeled as clouds. In addition to pure color characteristics, Roy et al. (Roy et al., 2001) tried a neural network approach with a wider range of variables for cloud segmentation. West et al. (West et al., 2014) also used a neural network to classify pixels. The features they used are colors and the distance of the pixel to the sun. Under lower-visibility conditions, aerosol and thin clouds tend to cause errors in cloud determination. To improve the accuracy of the single threshold method, Huo and Lu proposed an integrated method for cloud determination under low visibility conditions (Huo and Lu, 2009). The integrated cloud-determination algorithm uses fast Fourier transform, symmetrical image features, and self-adaptive thresholds. Li (Li et al., 2011) proposed a hybrid thresholding algorithm (HYTA) for cloud detection on ground-based color images, aiming at complementing fixed thresholding and adaptive thresholding algorithms. HYTA identifies the ratio image as either unimodal or bimodal according to its standard deviation. Then, the unimodal and bimodal images are handled by fixed and minimum cross entropy (MCE) thresholding algorithms, respectively. Kazantzidis (Kazantzidis et al., 2012) tuned multiple heuristic thresholds on RGB color components to detect clouds. The above mentioned works mostly consider the features extracted from each single pixel, but do not consider the local image patch and structure around the pixel. Bernecker et al. (Bernecker et al. 2013) used color and texture as features. After applying deep belief networks to learn the structure of the features, a random forest classifier is used to classify image patches into three classes: sky, cloud, and thick cloud. Bernecker et al. proposed to utilize information of image patch. However, they used fixed-size patches for training and classification without considering multiresolution information. Patches with sizes that

Atmos. Meas. Tech. Discuss., doi:10.5194/amt-2016-169, 2016
Manuscript under review for journal Atmos. Meas. Tech.
Published: 9 August 2016

Atmospheric Measurement Techniques Discussions

are too large would include features from both sky and clouds. On the other hands, patches with sizes that are too small might not include enough information to represent the appearance of the clouds.

In this paper, we propose to perform cloud detection via extracting features from local image patches with various sizes. Patches of different sizes extract information at different levels of resolution. For classification, we utilize multiple supervised learning techniques. We regard the cloud detection problem as a two-class classification problem. In other words, we classify each pixel in the image as cloud or non-cloud. The cloud models are learned through the training process. We consider classifiers including Support Vector Machine (SVM), random forest, and Bayesian classifier. To extract features from each pixel, we calculate the red and blue ratio (RBR) as well as the color components of various color models including RGB, HSV, and YCbCr. To take advantage of the clues provided by multiple classifiers and multi-level resolution, we employ a scheme to combine multiple classification results to further increase the cloud detection accuracy. The methodology, including the features and the classifiers, is elaborated in Section 2. In Section 3, the proposed system framework is validated using a set of experimental images with manually labeled ground truth. The experimental results using different classifiers are demonstrated and discussed. Finally, conclusions are made in Section 4.

2 Methodology

The proposed system framework is illustrated in Fig. 1. For each all-sky image, Hough line transform is performed first to detect the vertical line of the sun, which is caused by the CCD device when capturing all-sky images. The pixels on this line often has bright intensities and could be confused as cloud pixels. After detecting and eliminating the vertical line of the sun, the rest of the pixels in the image are classified as cloud or non-cloud. The input images are RGB color images. For each all-sky image, the color components in various color space are computed. The color models considered in this work include RGB, HSV, and YCbCr. In addition to the above mentioned color components, the red blue ratio (RBR) of each pixel is also calculated and considered as a feature. To perform pixel-wise classification, all the color components and the RBR of the local image patches around a pixel are

Atmos. Meas. Tech. Discuss., doi:10.5194/amt-2016-169, 2016
Manuscript under review for journal Atmos. Meas. Tech.
Published: 9 August 2016

collected and concatenated as a feature vector for the pixel. Training samples are obtained from manually labeled ground truth images.

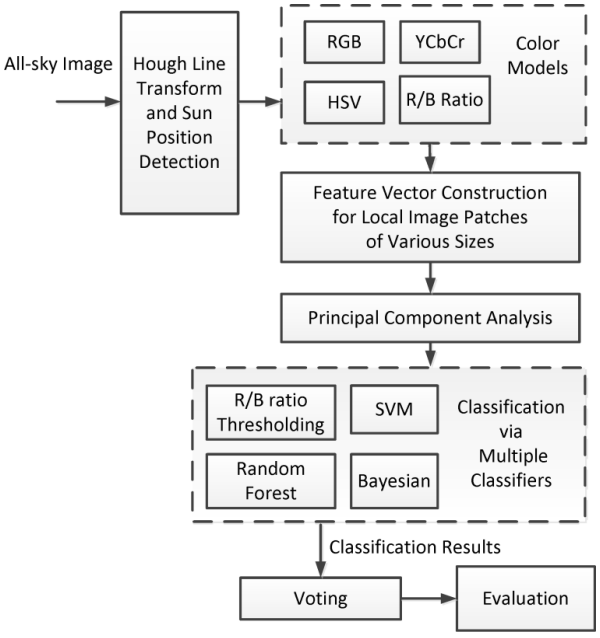

Fig. 1. System framework

2.1 Hough Line Transform and Sun Position Detection

Hough transform (Shapiro, 2011) is used to detect the vertical line of sun in an all-sky image. The procedure of detecting lines can be regarded as finding the coefficients of the line equations using a voting mechanism. The procedure of detecting lines via voting in the parameter space can be achieved by dividing the parameter space into grids. Because all the pixels satisfying a certain line equation would vote to the same grid, a high vote would appear in the corresponding grid in the parameter space. Hough transform re-parameterizes the line equation as $x\cos\theta + y\sin\theta = \rho$ to avoid uing the slope parameter for line equation y=*m*x+*b*. Because possible values for the slope parameter *m* ranges from minus infinity to infinity, it would be infeasible to find the slope parameter *m* via grid search. After, re-parameterizing the line equation, the range of the parameter ρ can be set according to the width and height of the image. And the range of the parameter θ is from -180° to 180°. Fig. 2 displays an example of Hough line detection on an image. After

Atmos. Meas. Tech. Discuss., doi:10.5194/amt-2016-169, 2016
Manuscript under review for journal Atmos. Meas. Tech.
Published: 9 August 2016

120 detecting the vertical line, the sun position is determined by accumulating the intensities of the
121 pixels along x direction in a window with width w_1. The position with the highest accumulated
122 intensity is the center of the sun. The pixels in the line window with a fixed width w_2 are
123 eliminated from the image. The pixels within the sun position and the line window with width w_2
124 are determined as non-cloud pixels and do not have to go through the subsequent classification
125 steps.
126

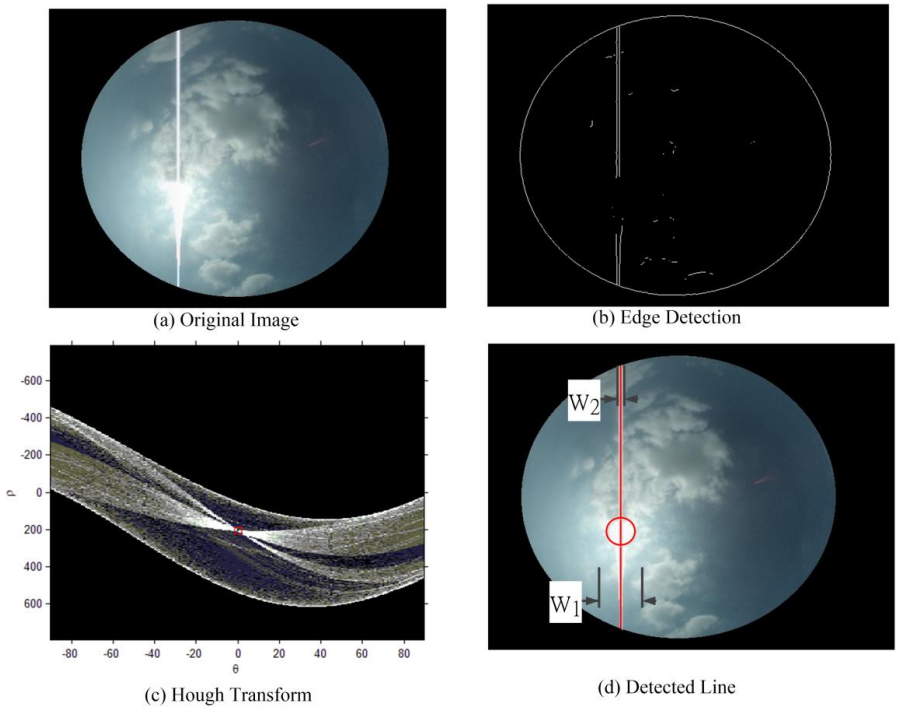

127
128 Fig. 2. Hough Line Detection and Sun Position Detection
129

130 2.2 Color Models

131 RGB is a very common color model, being used in most computer systems. It is an additive color
132 model based on tri-chromatic theory. RGB is easy to implement. However, it is non-linear with
133 visual perception, and the specification of colors is semi–intuitive. HSV is a color model that
134 describes colors in terms of hue, saturation and value components (Gonzalez, 2002). Hue is
135 expressed as a number from 0 to 360 degrees. The hue component of red starts at 0, green starts at

Atmos. Meas. Tech. Discuss., doi:10.5194/amt-2016-169, 2016
Manuscript under review for journal Atmos. Meas. Tech.
Published: 9 August 2016

Atmospheric Measurement Techniques Discussions

120, and blue starts at 240. Saturation is the amount of gray in the color. And the value component describes the brightness or intensity of the color. YCbCr is a color space used in video and digital photography systems. Y is the luminance component, and Cb and Cr are the blue-difference and red-difference chroma components.

2.3 Feature Vector Construction for Local Image Patches of Various Sizes

For each pixel, local image patches with various sizes are used to extract features. The size of the image patch at level i is $L_i \times L_i$, $i = 1 \cdots \ell$, where ℓ denotes the total number of levels. For each local image patch, the color components and the red to blue ratio (RBR) of all the pixels in the patch are concatenated to form a feature vector. Consequently, the dimension of the feature vector is $L_i \times L_i \times 10$. There are ℓ feature vectors constructed for each pixel.

2.4 Dimension Reduction

We apply Principal Component Analysis (PCA) (Duda et al., 2001) on the feature vectors to reduce their dimensions. Based on the assumption that the importance of the features lies in the variability of the data, PCA chooses principal components along the directions with the largest variance of the data distribution first. The principal components are a set of new orthogonal bases that can be used to re-express the data in order to reduce the correlation among different variables. Suppose that the original dataset has N_{Samples} samples and each sample has D_1 variables. The data matrix X is established with each sample as a column vector. Therefore the data matrix X has $N_{Samples}$ columns and D_1 rows. If we would like to reduce the feature dimension to D_2, then we need to select D_2 principal components. PCA constructs a matrix X^TX, which is a matrix proportional to the sample covariance matrix of the dataset X. The first D_2 eigenvectors of X^TX whose corresponding eigenvalues are largest are chosen as principal components. To determine the desired number of dimensionality D_2, we check the eigenvalue ratio $R_{Eigenvlaue}$

$$R_{Eigenvalue} = \frac{\sum_{k=1}^{D_2} |\lambda_k|}{\sum_{k=1}^{D_1} |\lambda_k|} \tag{1}$$

In Eq. (1), λ_k denotes the k^{th} Eigenvalue of X^TX. The first D_2 Eigenvectors are preserved so that

Atmos. Meas. Tech. Discuss., doi:10.5194/amt-2016-169, 2016
Manuscript under review for journal Atmos. Meas. Tech.
Published: 9 August 2016

Atmospheric Measurement Techniques Discussions

R_{Eigen} is larger than a threshold Thr_{PCA}. The selection of Thr_{PCA} is discussed in the experiments in Section 3.

2.5 Classifiers

2.5.1 Random Forest

Classification and Regression Tree (CART) is a systematic procedure that learns decision trees proposed by Breiman (Breiman et al., 1984). The splitting rules of the tree include an attribute value test at each node of the tree. Starting from the root node, all training data is used to split the root node. And the tree is built recursively. Considering all the possible splitting rules, CART would construct the tree by selecting the splitting rule that can maximize the impurity drop when a node is added. The impurity measures the condition of mixed class labels at each node. The goal is to make the class labels at each node as "pure" as possible. The splitting process stops when all the samples in a node have the same class label, or when the measure of purity at the child nodes cannot be improved compared with its parent node. After a decision tree is built, it might need to be pruned using a cross-validation procedure. The reason for pruning is that some branches of the tree might over-fit the training data. In our experiment, we use 10 fold cross validation. Instead of growing a single decision tree, random forest grows an ensemble of trees and lets them vote for the most popular class label. In this work, we adopt random split selection (Dietterich 1999) to build the ensemble of trees. At each node, the split is selected at random from the K best splits. The features for the split rules are randomly selected. It reduces the correlation between the trees and improves the efficiency of training.

2.5.2 Support Vector Machine

The Support Vector Machine (SVM) learns a set of hyperplanes that maximize the margins between the hyperplanes and the training samples in order to lower the classification error of unknown testing samples. The motivation of SVM is that an ideal decision boundary should have the largest distance to the nearest training sample of all the classes. However, it might be

Atmos. Meas. Tech. Discuss., doi:10.5194/amt-2016-169, 2016
Manuscript under review for journal Atmos. Meas. Tech.
Published: 9 August 2016

Atmospheric Measurement Techniques Discussions

infeasible to separate data samples using linear hyperplanes in practice. Therefore, soft margins and kernel functions are applied in the SVM in practice. We apply SVM with radial basis functions (RBF) as one of the classifiers in this work. For the details of SVM, please refer to the work by Cristianini and Shawe-Taylor (Cristianini and Shawe-Taylor, 2000).

2.5.3 Bayesian Classifier

Bayesian classifier aims at minimizing the probability of misclassification by classifying a sample x to the class ω_k with the largest posterior probability $P(\omega_k \mid x)$. Since the posterior probability $P(\omega_k \mid x)$ itself is unknown, we need to transform the problem using the probabilities that can be obtained via training samples. Bayesian classifier uses the Bayes' theorem to re-express the posterior probability using

$$P(\omega_k \mid x) = \frac{P(\omega_k)P(x \mid \omega_k)}{P(x)} \tag{2}$$

In Eq. (2), $P(\omega_k)$ denotes the prior probability, which is independent of the testing sample. In other words, $P(\omega_k)$ states how likely a pixel belongs to cloud or non-cloud regardless of its observed feature vector. It is possible to use meteorological conditions and weather forecast report to determine different prior probabilities $P(\omega_k)$ for each day. However, we use the same prior probabilities for both cloud and non-cloud classes for simplicity, and no meteorological information is required to be involved as prior knowledge in our decision process. The class conditional probability $P(x \mid \omega_k)$ in Eq. (2) can be learned from the training samples. We use Gaussian distributions

$$P(x \mid \omega_k) = \frac{1}{(2\pi)^{p/2} \mid \Sigma_k \mid^{1/2}} e^{-\frac{1}{2}(x-\mu_k)\Sigma_k(x-\mu_k)^T} \tag{3}$$

to model the class conditional probability $P(x \mid \omega_k)$ for each class. To learn the parameters of Gaussian functions, training samples from each class are used to calculate the sample mean vector μ_k and the sample covariance matrix Σ_k for the class. The probability of the

Atmos. Meas. Tech. Discuss., doi:10.5194/amt-2016-169, 2016
Manuscript under review for journal Atmos. Meas. Tech.
Published: 9 August 2016

Atmospheric Measurement Techniques Discussions

sample $P(x)$ in Eq. (2) does not depend on the class label and can be neglected in the decision process.

2.6 Combining Results of Multiple Level Neighborhoods and Classifiers

The concept of a multiple expert system is to take advantage of the clues provided by multiple classifiers. Instead of majority voting, we use a different voting scheme to combine the results of multiple-level patches and classifiers. As shown in Fig. 3, considering a 3×3 neighborhood around a pixel *p* at level *i*, its previous level $i-1$ and its next level $i+1$, voting is performed in the scale space of its $3\times3\times3$ neighborhood. The voting scheme takes into account the classification results from 4 classifiers: RBR thresholding, SVM, random forest, and Bayesian classifier. In other words, there are 27×4 votes for the pixel. Suppose x_{Level_i} denotes the feature vector of a pixel at level *i*, and the number of votes in the neighborhood classified as cloud at level *i* is denoted as $V_{cloud}(x_{Level_i})$. The decision for a pixel at level *i* is determined by $V_{cloud}(x_{Level_i}) > N_v$. In other words, if there are more than N_v votes in the $3\times3\times3$ neighborhood of a pixel at level *i*, the pixel is classified as a cloud pixel at this level. To combine the decision at different levels, the probability $P(x \in cloud \mid \underset{i=1\sim\ell}{Num}(x_{Level_i} \in cloud))$ is considered. Suppose $\underset{i=1\sim\ell}{Num}(x_{Level_i} \in cloud)$ denotes the number of levels at which the pixel is determined as cloud among all levels *i*=1 to ℓ. $P(x \in cloud \mid \underset{i=1\sim\ell}{Num}(x_{Level_i} \in cloud))$ states the probability of a pixel belonging to cloud given the information that the pixel is determined as cloud at $\underset{i=1\sim\ell}{Num}(x_{Level_i} \in cloud)$ levels. If $P(x \in cloud \mid \underset{i=1\sim\ell}{Num}(x_{Level_i} \in cloud))$ is larger than $P(x \in noncloud \mid \underset{i=1\sim\ell}{Num}(x_{Level_i} \in cloud))$, the final decision of the pixel would be a cloud pixel. The probability $P(x \in cloud \mid \underset{i=1\sim\ell}{Num}(x_{Level_i} \in cloud))$ can be expressed as Eq. (4). In Eq. (4), the term $P(\underset{i=1\sim\ell}{Num}(x_{Level_i} \in cloud))$ would not affect the decision. The prior probabilities $P(x \in cloud)$ and $P(x \in noncloud)$ are assumed to be equal as stated in Section

Atmos. Meas. Tech. Discuss., doi:10.5194/amt-2016-169, 2016
Manuscript under review for journal Atmos. Meas. Tech.
Published: 9 August 2016

Atmospheric Measurement Techniques Discussions

2.4.3. The likelihood term $P(\underset{i=1\sim\ell}{Num}(x_{Level_i} \in cloud) \mid x \in cloud)$ is learned from the training dataset by constructing the normalized histogram of $\underset{i=1\sim\ell}{Num}(x_{Level_i} \in cloud)$ using all ground truth cloud pixels.

$$P(x \in cloud \mid \underset{i=1\sim\ell}{Num}(x_{Level_i} \in cloud)) = \frac{P(x \in cloud)P(\underset{i=1\sim\ell}{Num}(x_{Level_i} \in cloud) \mid x \in cloud)}{P(\underset{i=1\sim\ell}{Num}(x_{Level_i} \in cloud))} \quad (4)$$

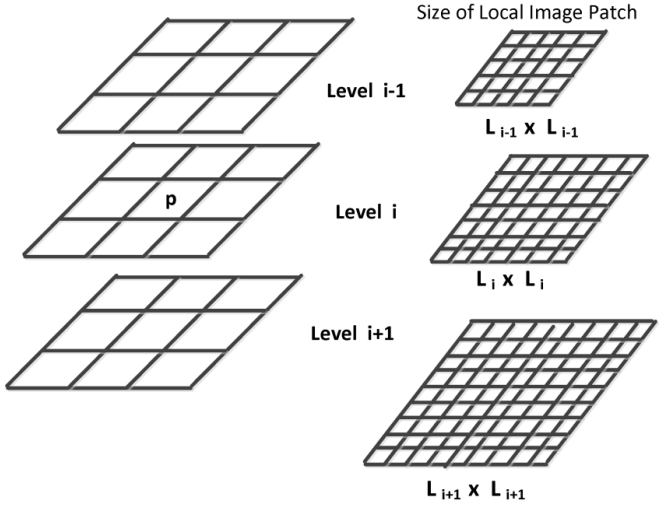

Fig. 3. Voting in the scale space of a $3\times3\times3$ neighborhood

3 Experimental Results

In this work, the device used to capture the all-sky images is the all-sky camera manufactured by the Santa Barbara Instrument Group (SBIG). The field of view is 185º. The focal length is 1.44 mm. And the focal ratio range is f/1.4–f/16. The resolution of the bitmap images is 640 x 480. We manually marked the ground truth of cloud pixels in 250 images for training and testing. These images are collected from January to June, 2014. With the ground truth labels of the images, we are able to calculate the detection accuracy at pixel level. We adopt 10-fold cross validation to calculate the average detection accuracy, precision and recall rate. The definitions of detection accuracy, precision and recall rate are listed in Eq. (5) to Eq. (7). True positive *TP* is the number of cloud pixels correctly detected. True negative *TN* is the number of non-cloud pixels that are correctly classified. False

Atmos. Meas. Tech. Discuss., doi:10.5194/amt-2016-169, 2016
Manuscript under review for journal Atmos. Meas. Tech.
Published: 9 August 2016

Atmospheric Measurement Techniques Discussions

positive *FP* is the number of non-cloud pixels that are incorrectly classified as clouds. False negative *FN* is the number of cloud pixels that are incorrectly classified as non-cloud.

$$Accuracy = \frac{TP + TN}{TP + TN + FP + FN} \quad (5)$$

$$Precision = \frac{TP}{TP + FP} \quad (6)$$

$$Recall = \frac{TP}{TP + FN} \quad (7)$$

According to Long (Long et al., 2006), the recommended RBR threshold is 0.6. However, in practice, the desired threshold varies due to different devices and weather conditions. Also, to avoid false positive detection at highlighted regions around the sun, it is better to employ an upper bound threshold. Therefore, two thresholds, Thr_{upper} and Thr_{lower}, are used in the experiments. A pixel is classified as cloud if its RBR is higher than Thr_{lower} and lower than Thr_{upper}. We perform experiments on several thresholds to select the best thresholds for our dataset. As shown in Fig. 4, we have observed that Thr_{lower} = 0.8 and Thr_{upper} = 0.9 yield the best detection accuracy for our dataset. In the rest of the experiments, we use RBR thresholding with Thr_{lower} = 0.8 and Thr_{upper} = 0.9 as a baseline method for comparison. However, even with the best selected RBR thresholds, the cloud detection result is not satisfying. The thresholds Thr_{lower} = 0.8 and Thr_{upper} = 0.9 might cause some false positives for certain images while causing some false negatives for other images. Therefore, neither raising or lowering the threshold could improve the detection results by thresholding.

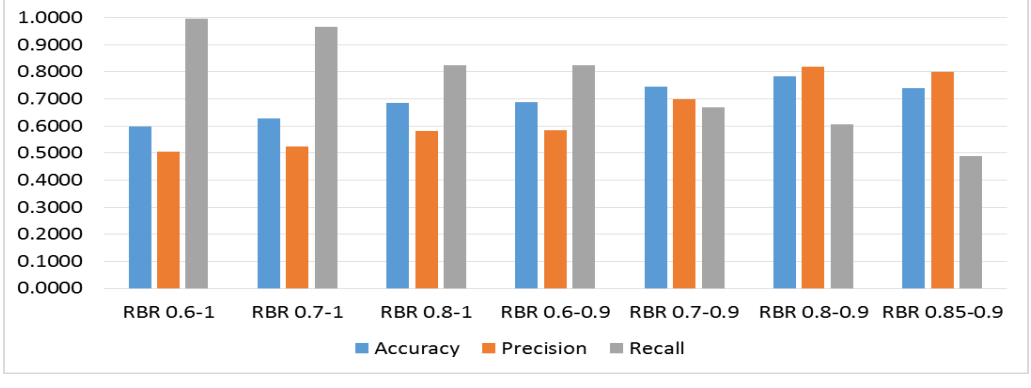

Fig. 4. Cloud detection accuracy using various RBR thresholds

Atmos. Meas. Tech. Discuss., doi:10.5194/amt-2016-169, 2016
Manuscript under review for journal Atmos. Meas. Tech.
Published: 9 August 2016

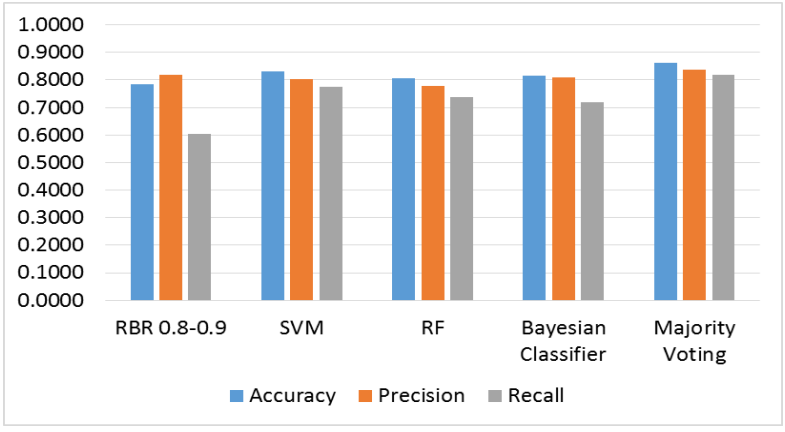

Fig. 5. Comparisons of detection accuracy using different classifiers with single pixel color information

To observe classification results of different classifiers, the detection accuracy of different classifiers based on single pixel color information are plotted in Fig. 5. Compared with other classifiers, RBR thresholding with Thr_{lower} = 0.8 and Thr_{upper} = 0.9 has the lowest detecction accuracy. Majority voting of the four detection methods can yield both better precision and recall rates. With voting schemes that combine the information from multiple classifiers, the accuracy can be enhanced compared with individual single classifiers. However, utilizing only single pixel color information is not sufficient to give satisfying detection accuracy. Applying features extracted from local image patch is able to further enhance the detection results.

When applying the proposed cloud detection method, we use five levels of local image patches with different sizes, i.e. ℓ=5. The size at each level is $L_1 = 5\times5$, $L_2 = 10\times10$, $L_3 = 15\times15$, $L_4 = 20\times20$, $L_5 = 25\times25$. To observe the effect of parameter Thr_{PCA} for dimension reduction at each level, we perform an experiment using feature vector constructed at each single level with SVM as the classifier for different settings of Thr_{PCA}. We plot the cross-validated detection accuracy in Fig. 6. From Fig. 6, we can observe that the detection accuracy at single level using SVM is highest for Thr_{PCA}=97% at levels L_1 and L_2. At levels L_3, L_4 and L_5, the parameter Thr_{PCA}=95% yields better results. Therefore, for levels L_1 and L_2, Thr_{PCA}=97% is selected; for levels L_3, L_4 and L_5, Thr_{PCA}=95% is selected.

Atmos. Meas. Tech. Discuss., doi:10.5194/amt-2016-169, 2016
Manuscript under review for journal Atmos. Meas. Tech.
Published: 9 August 2016

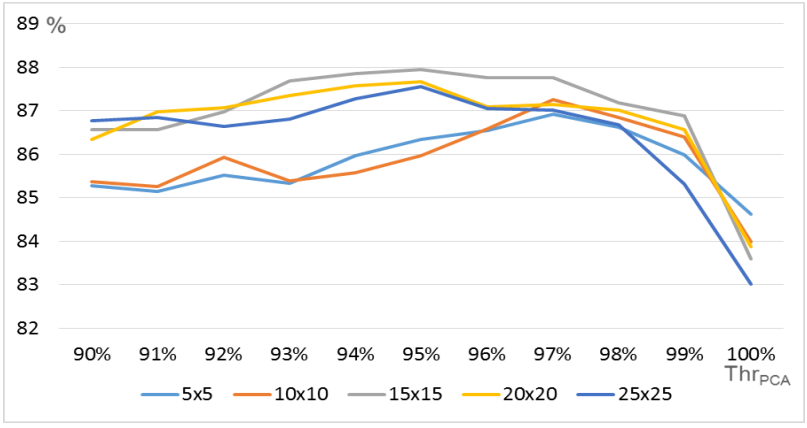

Fig. 6. Detection accuracy with different Thr_{PCA} settings at each level using SVM

To combine results of multiple level patches and classifiers, the threshold for voting N_v needs to be determined. The detection accuracy of combining the results using different N_v settings is plotted in Fig. 7. As shown in Fig. 7, when N_v ranges from 50 to 70, the detection accuracy is higher. We select N_v=57 for the proposed method.

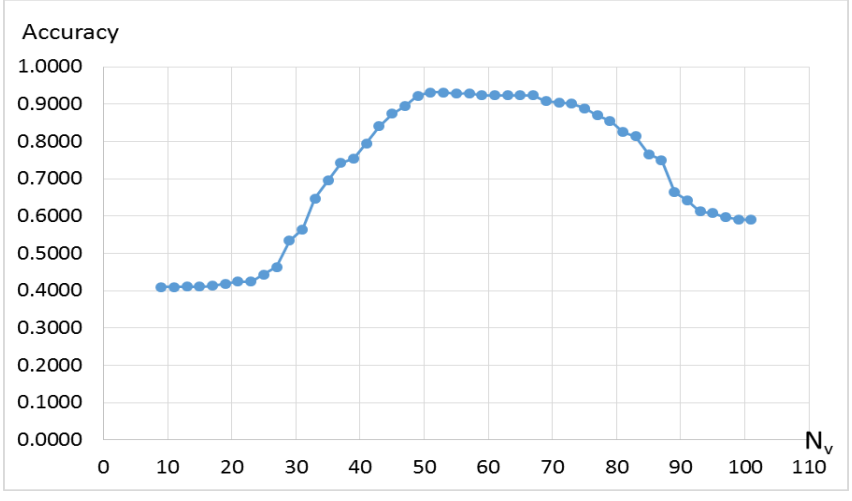

Fig. 7. Detection accuracy with different N_v settings

Atmos. Meas. Tech. Discuss., doi:10.5194/amt-2016-169, 2016
Manuscript under review for journal Atmos. Meas. Tech.
Published: 9 August 2016

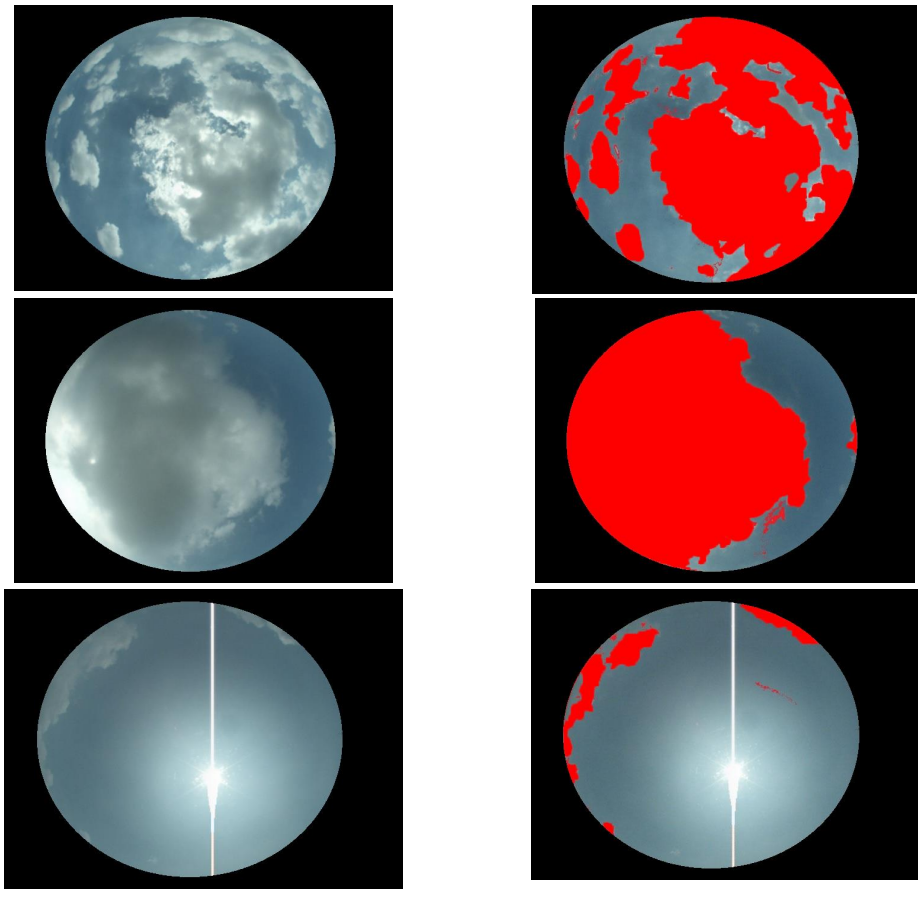

Fig. 8. Detection results of the proposed method

Selected cloud detection results are shown in Fig. 8. The proposed method using features from multi-scale local image patches can accurately detect clouds in the all-sky images. The pixels within the vertical line and the solar disk would not be detected as clouds even though their intensities are high. The Hough line detection and sun position detection successfully eliminated those pixels before performing classification. With the proposed multi-level local patch feature extraction mechanism and combination of multiple expert decision, the cloud pixels can be detected with satisfying accuracy.

To summarize the detection accuracy, the detection accuracy of various methods are plotted in Fig. 9. We compare the proposed method with ANN (Roy et al., 2001) and HYTA (Li et al., 2011). ANN utilized a feedforward back-propagation neural network to perform detection. HYTA employs dynamic thresholding based on minimum cross entropy when necessary. The ANN and HYTA methods

Atmos. Meas. Tech. Discuss., doi:10.5194/amt-2016-169, 2016
Manuscript under review for journal Atmos. Meas. Tech.
Published: 9 August 2016

outperform traditional RBR thresholding. Nevertheless, the accuracy of ANN and HYTA still has room for improvement. Using the single pixel color components described in Section 2.2 and utilizing SVM as the classifier can yield slightly improved accuracy compared with ANN and HYTA. Incorporating feature vector extracted from single level 15x15 neighborhood patch can further improve the accuracy compared with using only information from single pixel. The proposed method utilizing features extracted from multi-level neighborhood yields the best accuracy since multiscale information is considered.

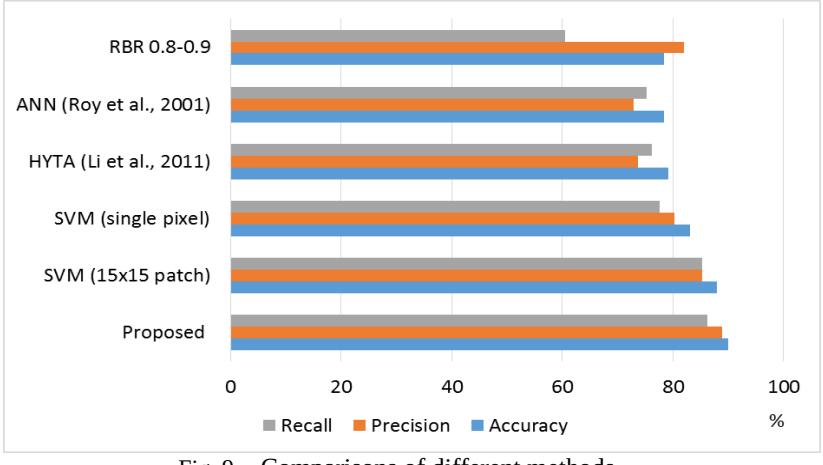

Fig. 9. Comparisons of different methods

4 Conclusions

With the development of all-sky cameras, the cloud conditions in the sky can be monitored and useful information can be extracted for solar irradiance prediction with refined spatial and temporal resolutions. Clouds play a critical role in affecting the amount of solar irradiance penetrating the atmosphere. With more accurate cloud detection schemes, subsequent prediction modules that forecast solar irradiance could benefit a lot from the enhanced detection results. In this work, supervised learning methods are utilized to train various classifiers that can distinguish cloud pixels from non-cloud pixels in all-sky images. The classifiers implemented in this work include RBR thresholding, SVM, random forest, and Bayesian classifier. We propose to use features extracted from multi-level local image patches with different sizes to include local

Atmos. Meas. Tech. Discuss., doi:10.5194/amt-2016-169, 2016
Manuscript under review for journal Atmos. Meas. Tech.
Published: 9 August 2016

Atmospheric Measurement Techniques Discussions

structure and multi-resolution information. Final decision is made according to multi-level classification results by various classifiers. A challenging dataset with ground truth labels is used to validate the detection schemes. In the experiments, we have shown that selecting a suitable RBR threshold for this challenging dataset is not feasible. Experiments have also shown that the detection schemes based on supervised learning perform better than both fixed and dynamic RBR thresholding. Combining the information of multiple classifiers using voting can improve the detection accuracy. It is also validated that using color information in multi-level local neighborhood instead of only a single pixel is very helpful to improve the detection accuracy.

Acknowledgements

The financial support provided by the Ministry of Science and Technology of Taiwan is gratefully acknowledged.

References

Bernecker, D., Riess, C., Christlein, V., Angelopoulou, E., Hornegger, J., 2013. Representation learning for cloud classification. Lecture Notes in Computer Science 8142, 395-404.

Breiman, L., Friedman, J. H., Olshen, R. A., Stone, C. J., 1984. Classification and regression trees. Monterey, CA: Wadsworth & Brooks/Cole Advanced Books & Software.

Calbo, J., Sabburg, J., 2008. Feature extraction from whole-sky ground-based images for cloud-type recognition. J. Atmos. Ocean. Tech. 25, 3-14.

Cazorla, A., Olmo, F. J., and Alados-Arboledas, L., 2008. Development of a sky imager for cloud cover assessment. J. Opt. Soc. Am. A. 25, 29-39.

Cheng, HY, Yu, C.C., 2015. Multi-Model Solar Irradiance Prediction Based on Automatic Cloud Classification. Energy 91, 579-587.

Cheng, H.Y., Yu C.C., 2015. Block based cloud classification with statistical features and distribution of local texture features. Atmospheric Measurement Techniques 8, 1173–1182.

Atmos. Meas. Tech. Discuss., doi:10.5194/amt-2016-169, 2016
Manuscript under review for journal Atmos. Meas. Tech.
Published: 9 August 2016

Atmospheric Measurement Techniques Discussions

360 Chow, C.W., Urquhart, B., Lave, M., Dominguez, A., Kleissl, J., Shields, J., Washom, B., 2011. Intra-hour
361 forecasting with a total sky imager at the UC San Diego solar energy testbed. Solar Energy 85,
362 2881-2893.

363 Cristianini N, Shawe-Taylor J. An introduction to support vector machines and other kernel-based learning
364 methods. Cambridge University Press, 2000.

365 Duda, R.O., Hart, P.E., Stork, D.G., 2001. Pattern classification. John Wiley & Sons, 2001; 2nd edn.

366 Feister, U. and Shields, J., 2005. Cloud and radiance measurements with the VIS/NIR daylight whole sky
367 imager at Lindenberg (Germany). Meteorol. Z. 14, 627-639.

368 Fu, C.L., Cheng, H.Y., 2013. Predicting solar irradiance with all-sky image features via regression. Solar
369 Energy 97, 537-550.

370 Gonzalez, R.C., Woods, R.E., 2002. Digital Image Processing 2nd Edition, Prentice Hall.

371 Gueymard, C.A., 2004. The sun's total and spectral irradiance for solar energy applications and solar
372 radiation models, Solar Energy 76 (4), 423-453.

373 Heinemann, D., Lorenz, E., Girodo, M., 2006. Solar Irradiance Forecasting for the Management of Solar
374 Energy Systems, Solar 2006, Denver, CO, USA.

375 Heinle, A., Macke, A., Srivastav, A., 2010. Automatic cloud classification of whole sky images. Atmos.
376 Measur. Technol. 3, 557-567.

377 Huo, J., Lu, D., 2009. Cloud determination of all-sky images under low visibility conditions. J. Atmos.
378 Ocean. Technol. 26 (10), 2172-2180.

379 Johnson, R., Hering W., Shields, J., 1989. Automated visibility and cloud cover measurements with a
380 solid-state imaging system. Tech. Rep., University of California, San Diego, Scripps Institution of
381 Oceanography, Marine Physical Laboratory, SIO Ref. 89-7, GL-TR-89-0061, 128.

382 Johnson, R., Shields, J., Koehler, T., 1991. Analysis and interpretation of simultaneous multi-station whole
383 sky imagery. Marine Physical Laboratory. Scripps Institution of Oceanography, University of California
384 San Diego, SIO 91-3, PL-TR-91-2214.

Atmos. Meas. Tech. Discuss., doi:10.5194/amt-2016-169, 2016
Manuscript under review for journal Atmos. Meas. Tech.
Published: 9 August 2016

Atmospheric Measurement Techniques Discussions

385 Kassianov, E., C. N. Long, and M. Ovtchinnikov, 2005. Cloud sky cover versus cloud fraction: Whole-sky
386 simulations and observations. J. Appl. Meteor. 44, 86-98.
387 Kazantzidis, A., Tzoumanikas, P., Bais, A.F., Fotopoulos, S., Economou, G., 2012. Cloud detection and
388 classification with the use of whole-sky ground-based images, Atmospheric Research 113, 80-88,
389 Kubota, M., T. Nagatsuma, and Y. Murayama, 2003: Evening corotating patches: A new type of aurora
390 observed by high sensitivity all-sky cameras in Alaska. Geophys. Res. Lett. 30, 1612.
391 Li, Z., M. C. Cribb, F.-L. Chang, and A. P. Trishchenko, 2004: Validation of MODIS-retrieved cloud
392 fractions using whole sky imager measurements at the three ARM sites. Proc. 14th ARMScience Team
393 Meeting, Albuquerque, NM, Atmospheric Radiation Measurement Program 6, 2-6.
394 Li, Q., Lu, W., Yang, J., 2011: A Hybrid Thresholding Algorithm for Cloud Detection on Ground-Based.
395 Journal of Atmospheric and Oceanic Technology 28, 1286–1296.
396 Long, C. N., Sabburg, J., Calb´o, J., and Pag`es, D., 2006. Retrieving cloud characteristics from
397 ground-based daytime color all-sky images. J. Atmos. Ocean. Tech. 23, 633-652.
398 Lorenz, E., Hurka, J., Heinemann, D., Beyer, H.G., 2009. Irradiance Forecasting for the Power Prediction
399 of Grid-Connected Photovoltaic Systems, IEEE J. of Selected Topics in Applied Earth Observations and
400 Remote Sensing 2, 2-10.
401 Marquez, M., Coimbra, C.F.M., 2011. Forecasting of global and direct solar irradiance using stochastic
402 learning methods, ground experiments and the NWS database. Solar Energy 85, 746-756.
403 Marquez, R., Coimbra, C.F.M., 2013. Intra-hour DNI forecasting based on cloud tracking image analysis,
404 Solar Energy 91, 327-336
405 Martínez-Chico, M., Batlles, F.J., Bosch, J.L., 2011. Cloud classification in a mediterranean location using
406 radiation data and sky images, Energy 36 (7), 4055-4062.
407 Perez, R., Ineichen, P., Moore, K., Kmiecik, M., Chain, C., George, R., Vignola, F., 2002. A new
408 operational model for satellite-derived irradiances: description and validation. Solar Energy 73,
409 307-317.
410 Perez, R., Kivalov, S., Schlemmer, J., Hemker Jr., K., Renne´, D., Hoff, T., 2010. Validation of short and
411 medium term operational solar radiation forecasts in the US. Solar Energy 84, 2161-2172.

Atmos. Meas. Tech. Discuss., doi:10.5194/amt-2016-169, 2016
Manuscript under review for journal Atmos. Meas. Tech.
Published: 9 August 2016

412 Pfister, G., McKenzie, R. L., Liley, J. B., Thomas, A., Forgan, B. W., and Long, C. N., 2003. Cloud
413 coverage based on all-sky imaging and its impact on surface solar irradiance. J. Appl. Meteorol. 42,
414 1421-1434.
415 Remund, J., Perez, R., Lorenz, E., 2008. Comparison of solar radiation forecasts for the USA. Proc. of the
416 23rd European PV Conference, 1.9-4.9, Valencia, Spain.
417 Roy, G., Hayman, S., Julian, W., 2001. Sky analysis from CCD images: cloud cover. Lighting Research and
418 Technology 33 (4), 211-222.
419 Sabburg, J., Wong, J., 1999. Evaluation of a Ground-Based Sky Camera System for Use in Surface
420 Irradiance Measurement. Journal of Atmospheric and Oceanic Technology 16, 752-759.
421 Shapiro, L. and George, C. S., 2001. Computer Vision. Prentice Books, Upper Saddle River.
422 Shields, J., Karr, M., Burden, A., Johnson, R., Hodgkiss, W., 2007. Continuing support of cloud free line of
423 sight determination including whole sky imaging of clouds. Final Report for ONR Contract
424 N00014-01-D-0043DO #13, Marine Physical Laboratory, Scripps Institution of Oceanography,
425 University of California San Diego, Technical Note 273.
426 Shields, J., Karr, M., Burden, A., Johnson, R., Mikuls, V., Streeter, J., Hodgkiss, W., 2009. Research toward
427 Multi-Site Characterization of Sky Obscuration by Clouds. Final Report for Grant N00244-07-1-009,
428 Marine Physical Laboratory, Scripps Institution of Oceanography, University of California San Diego,
429 Technical Note 274.
430 Tapakis, R., Charalambides, A.G., 2013. Equipment and methodologies for cloud detection and
431 classification: A review. Solar Energy 95, 392-430.
432 West, S.R., Rowe, D., Sayeef, S., Berry, A., 2014. Short-term irradiance forecasting using skycams:
433 Motivation and development. Solar Energy 110, 188–207.
434 Wood-Bradley, P., Zapata, J., Pye, J., 2012. Cloud tracking with optical flow for short-term solar forecasting.
435 50th conference of the Australian Solar Energy Society, Melbourne, December.
436